Journal of Alloys and Compounds 889 (2021) 161655

Contents lists available at ScienceDirect

Journal of Alloys and Compounds

journal homepage: www.elsevier.com/locate/jalcom

Effects of Ti substitution for Zr on the electrochemical characteristics and structure of AB_2-type Laves-phase alloys as metal hydride anodes

ChuBin Wan[a,b,*], R.V. Denys[b,c], V.A. Yartys[b,**]

[a] University of Science and Technology, Beijing 100083, China
[b] Institute for Energy Technology, P.O. Box 40, Kjeller NO-2027, Norway
[c] Hystorsys AS, P.O. Box 45, Kjeller NO-2027, Norway

ARTICLE INFO

Article history:
Received 29 June 2021
Received in revised form 11 August 2021
Accepted 18 August 2021
Available online 20 August 2021

Keywords:
Metal hydride anode
Laves phases
Neutron diffraction
Electrochemical performance
Hydrogen storage materials

ABSTRACT

The structural composition and electrochemical capacity of four AB_2 Laves-type intermetallic alloys with various Ti/Zr ratios ($Ti_xZr_{1-x}La_{0.03}Ni_{1.2}Mn_{0.7}V_{0.12}Fe_{0.12}$, x = 0.12, 0.15, 0.18, and 0.22) were investigated in this study. The alloys were characterized by X-ray diffraction, scanning electron microscopy and energy dispersive spectroscopy. These data revealed the coexistence of the main phase of the C15-type FCC Laves-type AB_2 compounds with a secondary La–Ni intermetallic that was present in minor amounts. Increasing the Ti substitution for Zr caused the gradual shrinkage of the unit cells of the C15 phase. The neutron powder diffraction studies demonstrated that in the trihydride (Ti, Zr, V)(Ni, Mn, Fe, V)$_2D_{3.2}$, D atoms filled A_2B_2 tetrahedra, whereas V atoms occupied not only conventional 16*d* sites but also partially replaced Zr/Ti at 8*a* sites. All studied alloys showed similar activation behaviors, wherein four cycles were required to realize the highest electrochemical capacity of the anodes. The Ti12/Zr88 alloy demonstrated excellent full discharge capacity that reached 466 mAh/g. The Ti22/Zr78 alloy electrode exhibited good cycling stability (retention rate of ~71%) after 500 cycles and a superior high-rate discharge capability (retention rate of ~71%) at a discharge current density of 400 mA/g. The cycling of the Ti22/Zr78 alloy electrode was studied by electrochemical impedance spectroscopy (EIS) to understand the reasons for the deterioration of cycling capacity, which was related with the pulverization of the alloys and increase in irreversible capacity.

© 2021 The Author(s). Published by Elsevier B.V.
CC_BY_4.0

1. Introduction

The Ni/MH (nickel hydride) batteries have for a long time been the most extensively used energy/power sources for hybrid electrical vehicles [1,2]. The AB_2 Laves-phase alloys are potential negative electrode materials for the rechargeable nickel hydride batteries [3,4]. However, AB_2 MH alloys have inferior activation performance, exhibit low rate capabilities and insufficient cycle durability [5]. In general, the AB_2 Laves-phase alloys that are used as anodes for Ni/MH batteries are multielement (Zr and Ti as A atoms and Cr, Ni, Mn, and V as B atoms), multiphase (Laves phases and other phase constituents), and disordered materials [6–8].

The effects of Ti substitution for Zr on the structure and performances of Zr-based AB_2-type alloys were strongly dependent on the used alloy system. Our earlier studies showed that battery anode (Zr, Ti)(Ni, Mn, V)$_2$ alloys contained three types of intermetallic phases, including C14, C15 Laves-type compounds, and BCC solid-solution phases [4,9,10]. Despite of the high mutual solubility of Ti and Zr, only trace amounts of Ti could substitute for Zr in AB_2-type Y–Zr–Fe alloys [11]. The increasing Ti concentration at the A site resulted in decreasing lattice parameters of the C15 phase and increasing plateau pressures. Du et al. [12] reported a decreasing lattice parameters of C15 and C14 phases in $Zr_{1-x}Ti_x(Ni_{0.6}Mn_{0.3}V_{0.1}Cr_{0.05})_2$ alloys caused by an increment in Ti concentration. In alloys, Ti substitution for Zr improves activation and high-rate discharge ability (HRD). However, cycling stability and HRD deteriorate at high Ti contents (x > 0.3). Huot et al. [13] reported that with the increasing discharge current, the alloys with C15-type structure demonstrated a large decrease in discharging capacity, whereas the alloys only containing the C14 phase did not significantly alter the discharge capacity. Shu et al. [14] found that in the $Zr_{1-x}Ti_x(NiMnVCr)_{2.1}$ alloys, the Ti substitution for Zr showed no obvious impact on the microstructure and activation performance but increased the discharging capacity. Given the excellent corrosion resistance of Ti, Ti additives improve

* Corresponding author at: University of Science and Technology, Beijing 100083, China.
** Corresponding author.
E-mail addresses: cbwan@ustb.edu.cn (C. Wan), volodymyr.yartys@ife.no (V.A. Yartys).

https://doi.org/10.1016/j.jallcom.2021.161655
0925-8388/© 2021 The Author(s). Published by Elsevier B.V.
CC_BY_4.0

charging/discharging cycle life and reduce the average capacity attenuation rate. Sun et al. [15,16] observed that the increasing amount of Ti additive resulted in the increasing abundance of the C14 Laves phases but lowering the content of C15 Laves phases and non-Laves phases. The discharging capacities of electrodes were closely dependent on the amount of the constituent Laves phase compounds.

The formation of Laves-phase structures is well known to be related to the average values of electron density and atomic radii. Many investigations have mostly concentrated on optimizing the C14/C15 phase abundance ratio and on introducing a secondary phase to enhance the electrochemical performances of AB_2 alloys [7,17,18]. Compared with C14-type alloys, the C15 structure offered a better HRD performance because of its enhanced hydrogen bulk diffusion rates, improved specific power, and a better performance at low temperature with the disadvantage of an inferior cycle life [18]. Moreover, Zr–Ni and Ti–Ni phases play important roles in improving battery performances, including activation, HRD, and cycle life [19–21].

Annealing [22–24] was known to change the abundances of Laves phases and non-Laves-type minor phases in AB_2 alloys without varying the total compositions [18]. With the aim of determining the effects of constituent phases on the performance of the AB_2 alloys, we prepared homogeneous alloys through the annealing while adding small amounts of La to the composition of the alloys to improve their activation. Furthermore, many works have been performed on the multielement alloys with various additives, including Cr [25], V [26], Li [27], and O [28], introduced into the AB_2 alloys. Hence, we believe that the introduction of multi-elemental additives can improve the performance of the developed alloys.

Although earlier performed studies showed interesting results, we expect to further improve the electrochemical performances by optimizing the Ti/Zr ratios. Considering that the atomic weight of Zr is considerably higher than that of Ti, the discharging capacity of the alloys was expected to be improved through the substitution of Zr by Ti. Moreover, the Zr substitution by Ti led to a decreasing stability of the alloy's hydride [16]. This increased the dynamics of hydrogen desorption from the formed hydrides. Meanwhile, a significantly smaller atomic radius of Ti than Zr resulted in the contracted unit cell volumes of the hydrogen storage phases. The hydrogen-storing and electrochemical capacity of AB_2 alloys were closely dependent on the abovementioned parameters, thus the improvements upon the Ti doping was expected to be achieved.

In the current work, the impact of Ti/Zr ratios in the annealed Zr-based C15-type AB_2 alloys was systematically studied to uncover a relationship between the phase- structural and chemical compositions and the electrochemical performances.

2. Experimental

2.1. Synthesis and annealing of the alloys

Four alloys with various Ti/Zr ratios ($Ti_xZr_{1-x}La_{0.03}Ni_{1.2}Mn_{0.7}V_{0.12}Fe_{0.12}$, x = 0.12, 0.15, 0.18, and 0.22) designated as Ti12/Zr88, Ti15/Zr85, Ti18/Zr82, and Ti22/Zr78 were synthesized by means of arc melting with enough constituent elements (the purity of each individual element was better than 99.7%). Considering that Mn is consumed at high temperatures because of evaporation, an excess of 4% Mn was charged into the initial mixtures. The arc melting was conducted by using a water-cooled copper hearth in an atmosphere of high-purity Ar (99.998%). The samples with weights of 10 g were melted several times to guarantee the homogeneity and uniformity of the alloys. The prepared alloy ingots were placed in an atmosphere of Ar into the sealed stainless steel tubes, followed by transferring into a furnace. The annealing of the as-cast alloys was carried out at 950 °C for 10 h, followed by quenching into cold water.

2.2. Structural and microstructural characterization of the annealed alloys

The X-ray diffractometery (XRD, Philips X′Pert Pro) was employed to determine the phase-structural compositions of the prepared samples. The XRD data were collected in the 2θ range of 20–80° with a step of 0.01° and a CuK_α as the radiation source (λ = 1.5406 Å). The XRD data were treated via the whole powder pattern fitting and Rietveld refinement approach by the General Structure Analysis System software [29]. The scanning electron microscopy (SEM) was performed by using a JEOL-JSM6320F equipped with energy dispersive spectroscopy (EDS) to measure the compositions and phase distribution.

The neutron powder diffraction (NPD) measurements were conducted at SINQ Neutron Source with an HRPT diffractometer at the Paul Scherrer Institute, Switzerland [30] operating in a high-intensity mode (λ = 1.494 Å; 2θ range of 3.8°–164.75° with 0.05°/step). The deuteride was prepared from the Ti15/Zr85 alloy in an atmosphere of gaseous D_2 in a stainless-steel holder (with the wall thickness of 0.2 mm and inner diameter of 6 mm) connected to a Sievert-type apparatus and employed as an in-situ NPD sample container. The Rietveld refinement of neutron diffraction data was conducted using a GSAS software [29].

2.3. Electrochemical measurements

The MH electrodes for the half-cell measurements were prepared for the electrochemical characterization. Our earlier article could be consulted for the details of the electrode preparation process [31]. The electrochemical performance was measured in a 3-electrode system (9 N KOH solution electrolyte) at ambient conditions. The system was composed of a working electrode (MH), a sintered counter electrode ($NiOOH/Ni(OH)_2$), and a reference electrode (Hg/HgO). The full activation of each electrode was carried out at a rate of 0.3 C by performing 10 charging–discharging runs. The HRD and cycling stability were assessed, and the cut-off potential of discharging was set at −0.74 V vs. the Hg/HgO electrode.

The electrochemical properties were measured with a VSP-BioLogic Electrochemical Workstation at ambient temperature. The electrochemical impedance spectroscopy (EIS) tests were carried out in the frequency range of 100 kHz to 1 mHz with an amplitude of 5 mV vs. the open circuit potential at 50% depth-of-discharge (DOD) state. The linear polarization profiles were collected in a narrow overpotential range of ± 5 mV. The potentiostatic discharge was performed at a constant anodic potential of E = −0.6 V (vs. Hg/HgO) for 3600 s at 100% state of charge. Note that these electrodes were already subjected to 10 activation cycles before the tests.

3. Results and discussion

3.1. XRD analysis and microstructural characterization

The studied alloys contain a cubic C15 Laves phase with a $MgCu_2$-type structure as the only phase constituent. The Rietveld refinement plots of the XRD data of the $Ti_xZr_{1-x}La_{0.03}Ni_{1.2}Mn_{0.7}V_{0.12}Fe_{0.12}$ (x = 0.12–0.22) are shown in Fig. 1(a–d). The unit cell parameters and phase abundances of the alloys were provided in Table 1. The calculated profiles of the studied alloys fit the experimental pattern very well. The goodness-of-fit values are low and fall in the range of 1.6–3.1. The above data demonstrate that the proposed model is reliable and accurate.

The data indicate that a homogeneous single-phase C15-type intermetallic can be obtained by optimizing the multielement composition. Notably, all studied alloys were subjected to 10 h of annealing at 950 °C. Hence, the annealing treatment and

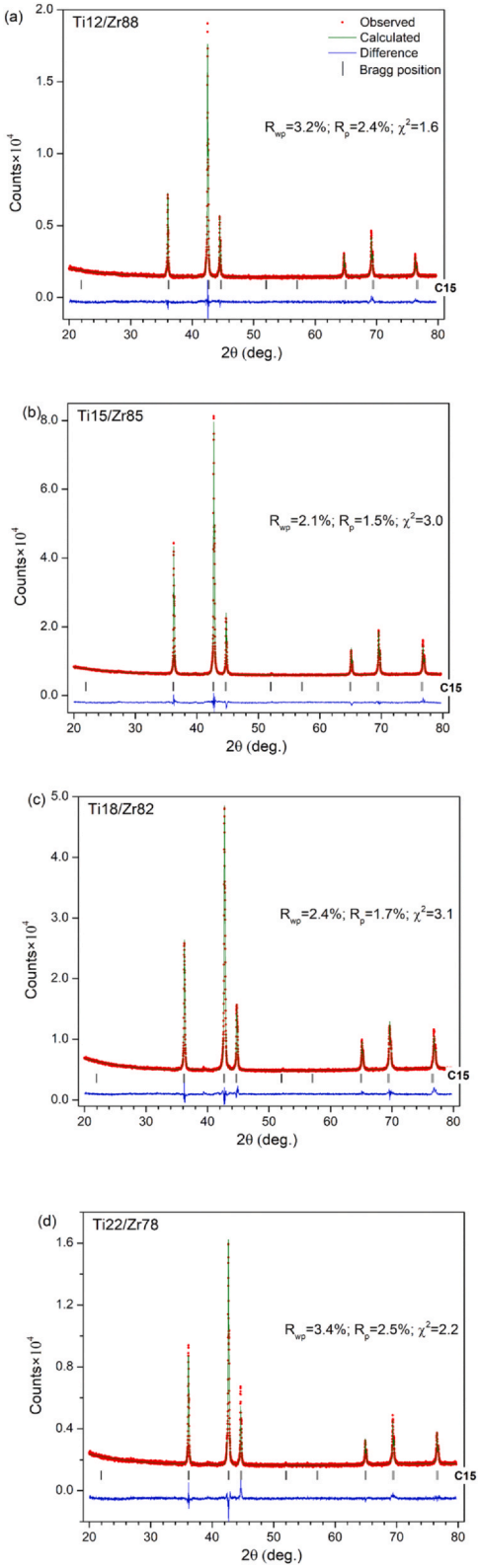

Fig. 1. Rietveld refinements of the XRD data for the annealed alloys. The vertical bars indicate the peak positions of the constituent C15 intermetallic phase.

optimization of the composition are necessary for producing homogeneous single C15 intermetallic alloys.

The lattice cell parameters of the C15 phases show a contraction following an increase in the Ti content of the studied alloys because smaller Ti atoms (r = 1.462 Å) substituted larger Zr (r = 1.602 Å) atoms in the structure. Both the unit cell parameter a and the volume V of the unit cells of the annealed alloys linearly decrease following an increase of Ti content in the intermetallics (Fig. S1, A and B, in the Supplementary Information file). This decrease follows a Vegard's law of proportionality vs content of Ti.

Table 1
Rietveld refinements results of the crystallographic parameters of the annealed alloys.

Alloys	Phase	Space group	Unit cell parameters	
			a, Å	V, Å^3
Ti12/Zr88	C15	$Fd\bar{3}m$	7.0599(1)	351.88(2)
Ti15/Zr85	C15	$Fd\bar{3}m$	7.0384(1)	348.67(2)
Ti18/Zr82	C15	$Fd\bar{3}m$	7.0227(1)	346.35(1)
Ti22/Zr78	C15	$Fd\bar{3}m$	7.0119(1)	344.75(2)

The microstructures of these alloys were characterized by SEM (Fig. 2). The chemical compositions at different locations in the same alloy, which are differentiated by the contrast levels in the images, were investigated through EDS, and the average concentrations of elements are summarized in Table 2. Additional details are listed in the Table S1 of the Supplementary Information file. All alloys are composed of a main AB_2 matrix (B) and a La–Ni phase with a bright contrast (A). In agreement with our earlier study, our present work confirmed that the addition of La leads to the formation of the La–Ni phase [10,32]. Detecting the presence of the La–Ni phase by using conventional XRD was impossible because the used amount of La was small (~1 at%).

As it can be seen in Table S2, a very good agreement between the aimed and obtained composition measured by EDS analysis has been achieved. As excellent agreement between these two sets of data is obvious for the Ti15/Zr85 alloy, deuteride of which has been studied by neutron powder diffraction.

XRD characterization was performed on the alloy electrodes after a long charge–discharge cycling to study the structural changes that have occurred during the testing. The refinements data are shown in Table S3. Only the C15 phase exists in the alloys that were cycled for 30 and 500 cycles. No hydride phases are found in the cycled alloys. This result indicates that the residual H, which can be potentially present in the cycled alloy, is not the reason for the cycling deterioration. The components of the main phase in the electrodes have not undergone oxidation or hydroxide formation even after 500 cycles. This result suggests that the formation of oxides or hydroxides does not account for the cycle degradation of the studied alloys.

Comparing the lattice constants of the annealed alloys reveals that the cycled alloys show only very small variations during the cycling. As shown in Table S3, in all studied alloys, the values of the unit cell parameters of the C15 phase remain almost unchanged (maximum difference 0.05%) during 500 charge–discharge cycles. This situation indicates that all the studied alloys show a good ability to retain the lattice stability during a long cycling in a KOH solution, when undergoing formation and decomposition of the corresponding hydrides.

3.2. NPD studies on the alloy deuteride

The activation of the initial Ti15/Zr85 alloy was conducted in vacuum at 573 K. After that the alloys was charged for 24 h with D_2 gas (99.8% purity) at ambient temperature and at D_2 pressure of 5 bar. Rapid deuteration was completed within 1 h. No addition cycling was conducted, and the sample was used in the initial charged state for the NPD investigation. On the basis of the variation in the monitoring the pressure variations in the studied system, the concentration of deuterium in the synthesized deuteride was evaluated to be 3.2 at. D/f.u. AB_2.

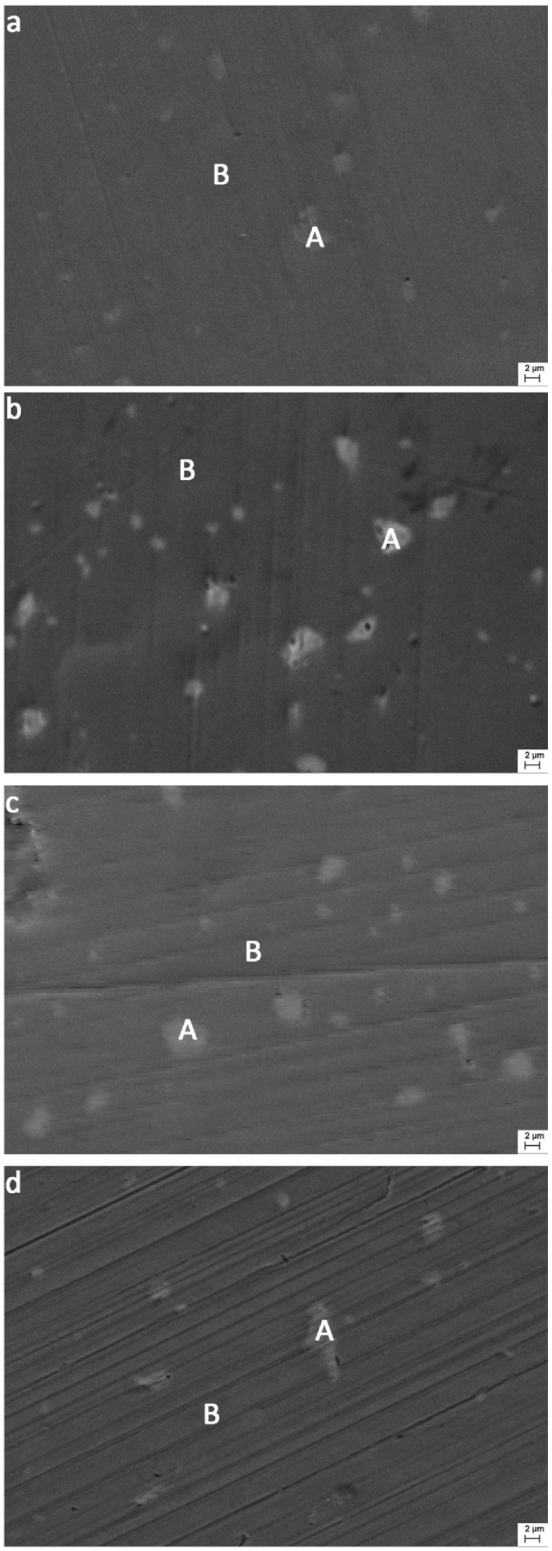

Fig. 2. SEM images of the annealed alloys, Ti12/Zr88 (a), Ti15/Zr85 (b), Ti18/Zr82 (c), and Ti22/Zr78 (d).

The neutron diffraction profiles for the Ti15/Zr85 alloy deuteride obtained through experimental measurements at 300 K and calculated profiles are shown in Fig. 3. The experimental diffraction profiles are assigned to the cubic C15-type hydride structure (space group $Fd\bar{3}m$) with the 8*a* site filled by the Ti, Zr, and V atoms and the 16*d* site occupied by the Ni, Mn, Fe, and V atoms in the deuteride. The 8*a* and 16*d* sites are occupied by the V atoms in the alloy deuteride (Table 3). As described in our earlier publication [32], vanadium can be partially located at the A site due to the chemical similarity of Ti and V as reflected by the formation of the isostructural dihydrides (Ti,V)H_2 with unlimited solubility between Ti and V.

The positions and occupancies of the D atoms were determined from the refinements performed for the $AB_2D_{3.2}$ deuteride of the Ti15/Zr85 alloy. The D atoms in the C15-type hydride $AB_2H_x(D)_x$ are capable of occupying 3 types of interstitial sites: 96*g* (A_2B_2), 32*e* (AB_3), and 8*b* (B_4). In the initial refinements, all these three types of sites were considered. However, only the 96*g* sites were verified to be occupied by D atoms, with refined D content of 3.2 atoms per formula unit AB_2D_x, while 32*e* and 8*b* sites remained vacant in the structure. This value is in excellent agreement with the synthesis data. Indeed, within an experimental error limit, the refined value of *x* is in agreement with that for the $AB_2D_{3.2}$ deuteride determined from the deuterium absorption measurements.

In the crystal structure of the $AB_2D_{3.2}$ deuteride the A_2B_2 tetrahedra are partially occupied by D atoms. Observed at 300 K unique occupancy of the 96*g* sites (*x*, *x*, *z*) by D atoms is in a good agreement with the usual trend reported for the Laves type Zr-based AB_2 hydrides, wherein the *g* sites are the only occupied by H(D) atoms sites at medium hydrogen contents close to 3 at.H / f.u. AB_2 [32,33].

Table 3 presents crystallographic data of the $AB_2D_{2.9-3.2}$ deuterides. The crystallographic data for the $AB_2D_{2.9}$ deuteride (atomic ratio Ti/Zr = 0.2/0.8) [32] are also listed in Table 3 for comparison. The *x* and *z* positional parameters of the D atoms in the 96*g* sites are similar to those for both deuterides [present study and reference 32]. The structural data for the $AB_2D_{3.2}$ deuteride at 300 K shows that the closest distances between the D atoms positions are r_{g1} = 1.193 (4) Å and r_{g2} = 1.305 (7) Å with a very small difference from the values for $AB_2D_{2.9}$ (r_{g1} = 1.174 [2] and r_{g2} = 1.314 [3] Å). These sites, however, are never simultaneously occupied because of the blocking of the filling of the neighboring sites with H–H distances that are shorter than 1.8–2.0 Å. The hexagons can be identified in the sub-lattice of the *g* sites in the Laves phases with cubic structure [34], and in these hexagons the first-nearest sites are located at a distance of r_{g1}, while r_{g2} features the second-nearest distances in the hexagon. The distances between the occupied by D atoms positions and surrounding metal atoms are 2.015 (4) and 2.030 (4) Å for 8*a* sites (metal atoms) and 1.740 (2) Å for the 16*d* sites (metal atoms) in D-Ti/Zr/V and D-Ni/Mn/Fe/V (as compared with 1.997 and 2.013 Å for 8*a* site and 1.739 Å for 16*d* sites, respectively, in the reference publication).

3.3. Electrochemical performance and EIS studies

The experimental data of SEM and XRD studies indicate that all the studied alloys have identical phase-structural compositions, a C15-type Laves phase (main phase), and a La–Ni intermetallic (minor phase). The activation of the studied alloys is not affected by the different ratios of Ti and Zr (the activation process is supposed to be completed when the discharge capacity reaches 98% of the maximum capacity) given that all studied alloys show excellent performance and finish activation within the first 4 cycles as a result of the catalyzing effect of the La–Ni intermetallic on the electrochemical charging.

Fig. 4a shows that in the studied alloys, the changes in Ti content significantly affect electrochemical storage capacity. During the first 10 runs, the discharge capacities of the studied alloys exhibit maximum values within a range of 335–385 mAh/g at a charge–discharge (C/D) current density of 100 mA/g. After the activation cycling, the discharging capacity of the Ti12/Zr88 alloy reaches 376 mAh/g, whereas that of the Ti15/Zr85 alloy rises to 385 mAh/g, which is the maximum discharging capacity among the studied alloys.

Table 2
Summary of the EDS characterization data. Elemental content is in atomic %.

Alloys	Loca-tion	Ti	Zr	Ni	Mn	V	Fe	La	Phases
Ti12/Zr88	A	0	0	49(3)	0	0	0	51(2)	LaNi
	B	4.3(0)	27.2(2)	40.2(8)	21.5(1)	3.3(2)	3.5(1)	0	AB_2
Ti15/Zr85	A	0	0	49(1)	0	0	0	51(1)	LaNi
	B	5.2(6)	28.0(1)	38.3(7)	21.4(8)	3.5(3)	3.6(7)	0	AB_2
Ti18/Zr82	A	0	0	50.2(6)	0	0	0	49.8(6)	LaNi
	B	6.2(9)	25.0(1)	40.0(2)	20.7(2)	4(1)	4.1(3)	0	AB_2
Ti22/Zr78	A	0	0	50(1)	0	0	0	50(1)	LaNi
	B	7.0(5)	25.0(1)	39.0(3)	20.3(3)	4(1)	4.7(6)	0	AB_2

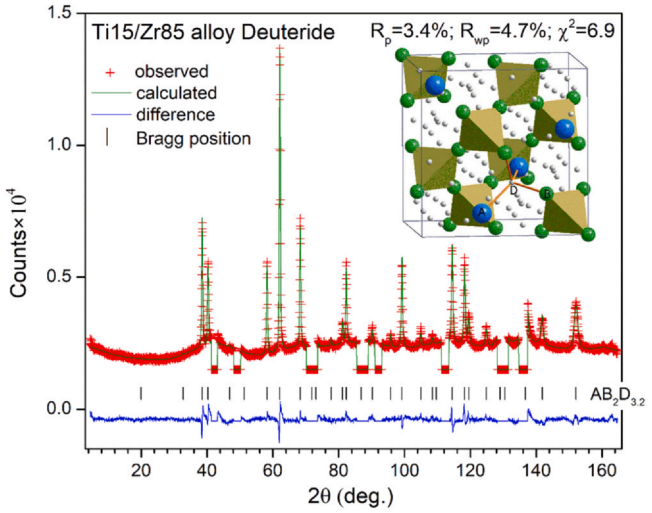

Fig. 3. Whole profile Rietveld refinements of the neutron powder diffraction pattern of the Ti15/Zr85 alloy deuteride $AB_2D_{3.2}$. The peaks of the stainless-steel sample container were eliminated from the refinements. Insert: The crystal structure of the FCC $AB_2D_{3.2}$ deuteride. A, B, and D represent Ti/Zr/V (8*a*), Ni/Mn/Fe/V (16*d*), and D(H) (96*g*) atoms, respectively. The spatial framework for B_4 tetrahedra is also displayed.

With increasing Ti content, the maximum discharge capacities of the alloys gradually decline. The discharge capacity of the Ti22/Zr78 alloy is low and is close to 335 mAh/g. As presented in Fig. 4b, the initial discharge capacities of Ti12/Zr88 and Ti15/Zr85 alloys are considerably higher (~14%) than those of the Ti18/Zr82 and Ti22/Zr78 alloys containing the higher amounts of Ti. This indicates that the maximum discharge capacities can be reached by optimizing the contents of Ti and Zr in the AB_2 alloys.

The data characterizing the cycling stability at various Ti contents in the alloys at the C/D current density of 300 mA/g (1 C) are presented in Fig. 4b. Although the Ti12/Zr88 and Ti15/Zr85 alloys present relatively high discharge capacities, they both show a rapid degradation with the increasing cycling. At the same time, the Ti22/Zr78 alloy exhibits a relatively slow decline in the discharge capacity after 500 C/D cycles. The cycling stability of the studied electrodes continuously enhances with the increase in Ti content. After 500 C/D cycles, the Ti22/Zr78 alloy shows a reversible capacity of approximately ~200 mAh/g, which is approximately 71% of its initial discharge capacity. The Ti22/Zr78 alloy electrode shows a superior cycling stability. We propose that the reason for the high cycle life of the Ti22/Zr78 alloy electrode is a superior corrosion resistance of titanium [14]. The formation of Ti oxide film on the alloy's surface in the charging/discharging cycles will furthermore inhibit the dissolution of the other present metal elements, Mn, Ni, and V.

Fig. 5 displays that the HRD performance of the annealed alloys as related to the applied potential and discharge current density. The maximum discharge capacity was obtained at the lowest applied current density rate of 10 mA/g, and it well corresponded to the hydrogen storage capacity of the annealed alloys. As an example, the full discharge capacity of the Ti15/Zr85 alloy is 456 mAh/g, which is equivalent to 1.63 wt% H and is attainable for the $AB_2H_{3.14}$ hydride. This value well agrees with the value for the $AB_2D_{3.2}$ deuteride determined from the neutron diffraction studies and in the absorption experiments of deuterium gas.

The discharge capacity drops from 380 mAh/g to 250 mAh/g, following by an increase in discharge current densities from 50 mA/g to 800 mA/g. Notably, all studied alloys show broad and flat discharge plateaux. A nearly constant voltage can be maintained for the alloy electrodes during their discharge, demonstrating their good potential for the use in battery applications.

A diagram comparing the HRD performances of the Ti-substituted alloys is provided in Fig. 4c. In this diagram, the HRD performance is depicted as a function of discharging current densities, which spanned a range from 10 mA/g to 800 mA/g. All the alloys were studied after the completion of 10 activation cycles. All the curves exhibit a similar shape over the whole applied discharge current density range. At the lowest current density (10 mA/g), the full measured discharge capacities are within the range of 384–466 mAh/g (Table 4). The full discharge capacity first decreases, which is followed by a slight increase with enhancing the Ti content. As shown in the Table 4, at a high current density of 400 mAh/g, the HRD performance of the Ti22/Zr78 alloy electrode is superior and is followed by that of the Ti18/Zr82, Ti15/Zr85, and Ti12/Zr88 alloy electrodes.

The discharge capacity is well known to be related both to hydrogen-storage properties and to the electrochemical kinetics of

Table 3
Crystallographic data for the $AB_2D_{3.2}$ and $AB_2D_{2.9}$ [32] deuterides from the Rietveld refinements of the neutron powder diffraction data.

Atomic positions	Crystal structure parameters	(Ti,Zr,V) (Ni,Mn,Fe,V)$_2$D$_{3.2}$ (Ti/Zr=0.15/0.85)	(Ti,Zr,V) (Ni,Mn,Fe,V)$_2$D$_{2.9}$ (Ti/Zr=0.2/0.8)
	a (Å)	7.5450(1)	7.5072(1)
	V (Å^3)	429.51(2)	423.08(2)
Ti/Zr/V	Occupancy	0.144/0.819/0.035(2)	0.213/0.751/0.036(2)
8*a*:1/8,1/8,1/8	U_{iso} × 100 (Å^2)	0.58(5)	0.77(6)
Ni/Mn/Fe/V	Occupancy	0.564/0.338/0.058/0.040(4)	0.564/0.338/0.058/0.040(5)
16*d*: 1/2,1/2,1/2	U_{iso} × 100 (Å^2)	1.17(4)	1.64(5)
D	Occupancy	0.267(2)	0.239(1)
96*g* (x, x, z)	U_{iso} × 100 (Å^2)	3.20(1)	3.76(9)
	x, z	0.0639(4), 0.8703(5)	0.0631(4), 0.8716(6)
D content	–	3.19(2) at.D/f.u.	2.87(1) at.D/f.u.

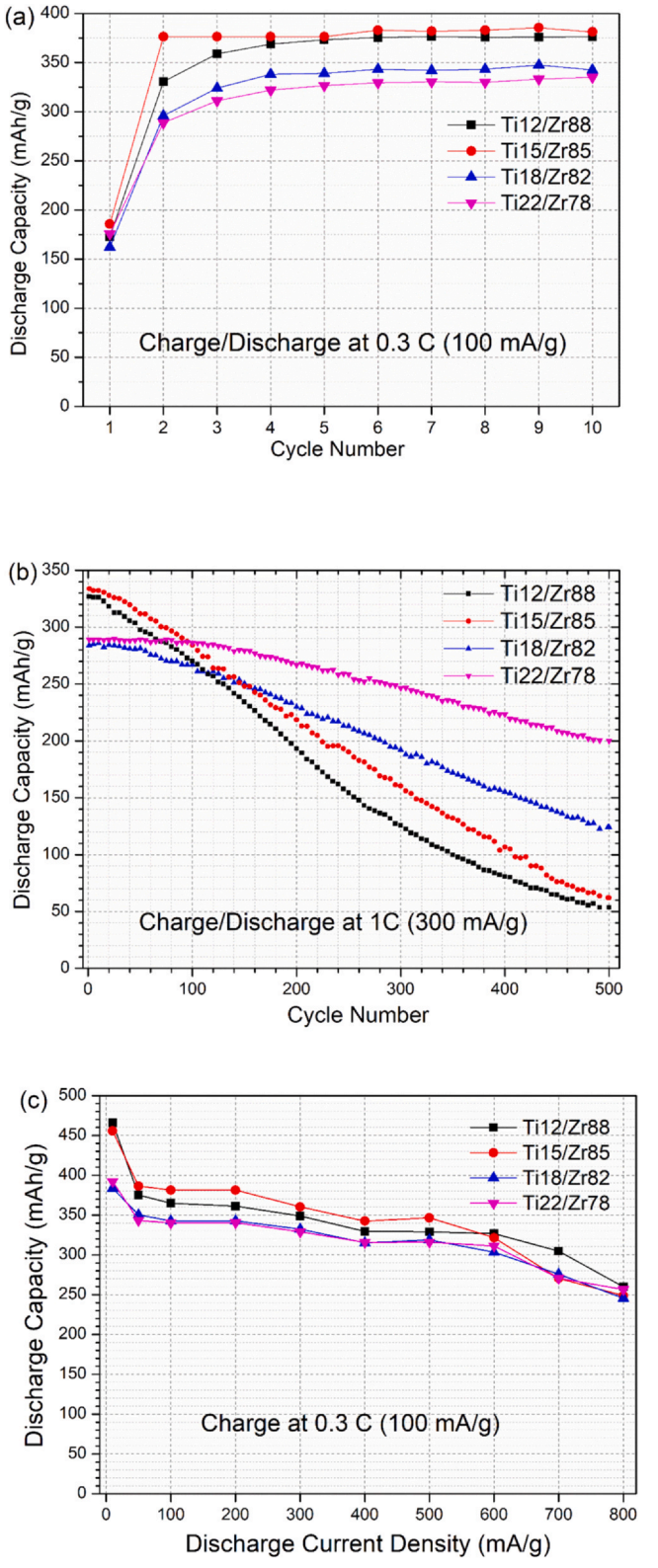

Fig. 4. Activation performance during the first 10 cycles (a), cycling stability (b), and HRD (c) of the annealed alloys after 10 activation cycles.

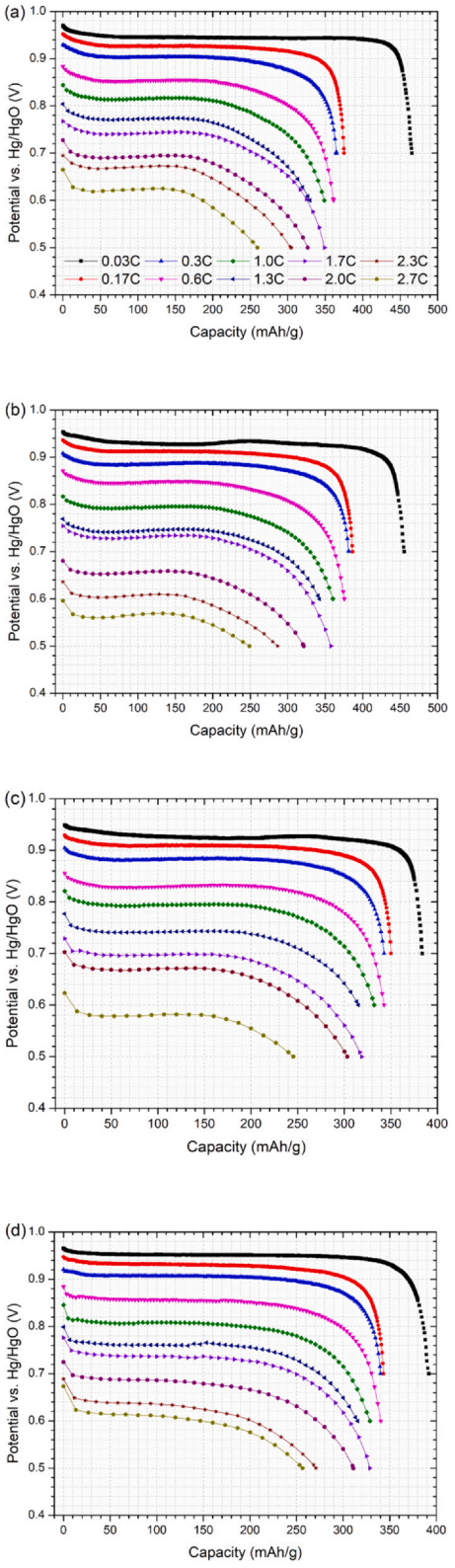

Fig. 5. High-rate discharge capacities of the annealed Ti12/Zr88 (a), Ti15/Zr85 (b), Ti18/Zr82 (c), and Ti22/Zr78 (d) alloys shown as the relationships between the applied potential and discharge capacity.

hydrogen oxidation. The electrochemical kinetics characteristics of the alloy electrodes are reflected by the HRD performance. In general, the HRD of the electrode alloy correlates with the features of the bulk material and, also, with the electrothermal surface behaviors of the alloys [5,35,36]. Hence, the potentiostatic discharge and linear polarization tests were conducted on the studied alloy electrodes to investigate their kinetics. The details of the measurements have been described in our earlier work [32], and the obtained data are displayed in Table 4 and Fig. 6. As the Ti content in the studied electrodes increases, the *D* value decreases and then increases, whereas I_0 exhibits the opposite trend. Therefore, in this

Table 4
Summary of electrochemical performance data and EIS results ($S_n[\%] = C_n/C_{max}$, and $HRD_n[\%] = C_n/C_{max}$).

Alloy	C_{max} (mAh/g)	S_{500} (%)	$HRD_{1.3C}$ (%)	D ($\times 10^{-10}$ cm^2/s)	I_0 (mA/g)	R_{ct} (Ω)
Ti12/Zr88	466	16.4	60.1	8.0	58.9	1.496
Ti15/Zr85	456	18.6	61.5	5.5	69.9	1.323
Ti18/Zr82	384	42.7	67.7	7.1	66.6	1.121
Ti22/Zr78	392	70.7	71.4	14.5	57.0	0.809

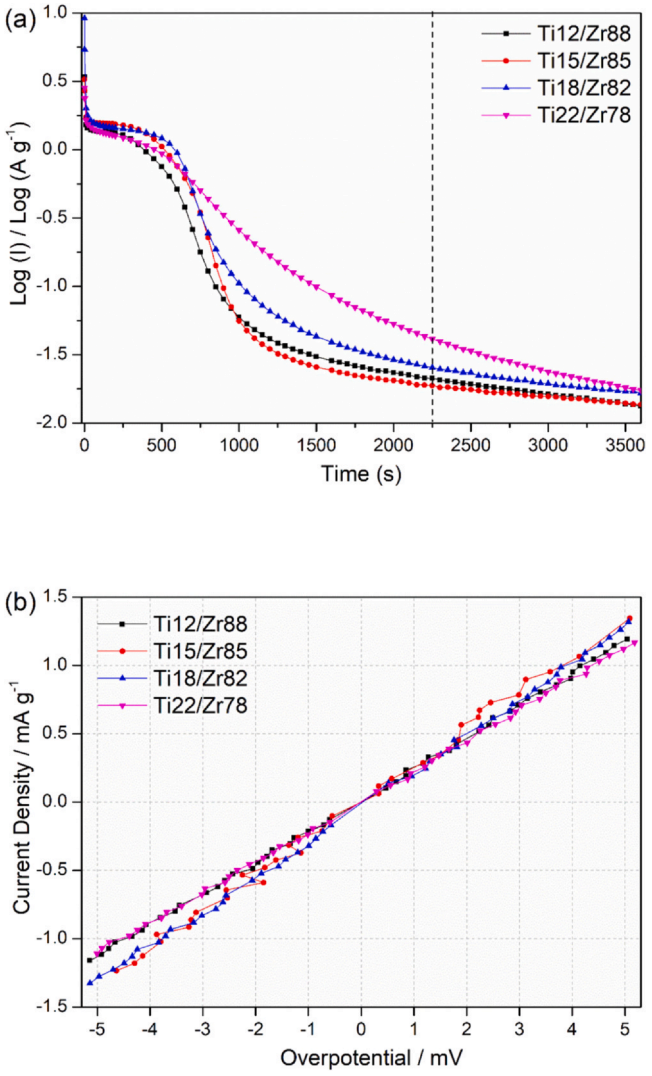

Fig. 6. Semilogarithmic profiles (a) of anodic current vs. time and linear polarization profiles (b) of the annealed alloy electrodes measured at room temperature with 50% DOD.

work, the enhancement in HRD may originate from the increasing bulk diffusion coefficient of hydrogen atoms, particularly for the alloys with high Ti contents. Considering that the studied alloys have the same La contents and similar phase compositions, the increase in D must originate from the synergetic effect of the C15 phase and the La–Ni phase.

The surface reaction features were further investigated by EIS at ambient temperature. The Cole–Cole plots are shown in Fig. S2, and the reaction resistances computed from the impedance spectra are shown in Tables 4 and S4. A variation in the reaction resistance R_{ct} is generated by the changing alloy surface reactivity and changing the surface reaction area [37]. With increasing Ti content, R_{ct} decreases

Table 5
Summary of the EIS results for the cycled Ti22/Zr78 alloy electrode.

Cycles number (N)	D ($\times 10^{-10}$ cm^2/s)	I_0 (mA/g)	R_1 (Ω)	R_2 (Ω)	R_3 (Ω)	R_{ct} (Ω)
10	14.5	57.0	0.046	3.795	0.376	0.920
100	16.3	65.3	0.047	3.366	0.229	0.264
350	14.2	52.7	0.085	3.386	1.168	1.343
500	11.9	53.0	0.092	3.404	0.967	0.725

continuously in agreement with the HRD order for the studied electrodes. Therefore, the improvement in HRD may also be ascribed to the improved reactivity of the alloy's surface due to the Ti substitution for Zr.

3.4. Electrochemical kinetics and EIS studies of the cycled alloys

We cycled the Ti22/Zr78 alloy electrode during the potentiostatic discharge experiments and performed linear polarization measurements to investigate the effects of cycling on its electrochemical kinetics.

As shown in Table 5 and Fig. S3, with the progression of cycling, D and I_0 increase after 100 cycles and then decrease. We reported similar results for $Ti_{0.2}Zr_{0.8}La_{0-0.05}Ni_{1.2}Mn_{0.7}V_{0.12}Fe_{0.12}$ alloys in our earlier publication [32]. D and I_0 reflect the electrochemical reactivity of an alloy. For a particular electrode material, a high electrochemical capacity should lead to the high values of D and I_0. However, D and I_0 are influenced by the changing size of the reaction surface area originating from the decrepitation of the alloy's particles. Therefore, their values cannot directly reflect the capacity loss of the cycled electrodes of the pulverized alloy particles, as the pulverization can improve the diffusion paths for H atoms. In present study, the electrode that was cycled for 100 times displayed a relatively higher discharge capacity than the electrodes that were cycled for longer times and obtained a higher reaction area than the electrodes that were cycled 10 times; thus, its D and I_0 can reach the higher values with cycling. Although the reaction area continuously increases with the increasing number of cycles, a relatively significant capacity loss causes eventual reduction of the D and I_0 values.

The EIS Cole–Cole plots are shown in Fig. 7, and the resistances obtained from the impedance spectra are displayed in Table 5. The equivalent circuit used for the fitting consists of 4 parts: two resistive components (R_2 and R_{ct}), electrolyte resistance (R1), and a Warburg term (W).

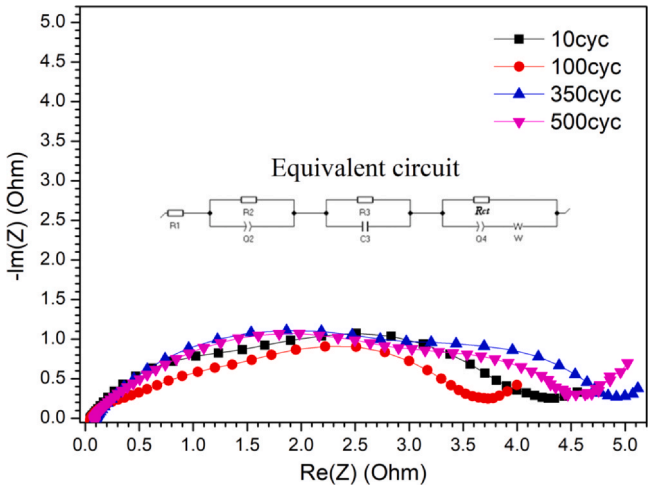

Fig. 7. Cole–Cole plots of the electrochemical impedance spectra acquired at 298 K for the cycled Ti22/Zr78 alloy electrodes.

R_1 indicates the resistance of the electrolyte between the reference and working electrodes [37]. R_2 mainly includes the contact resistance between a current collector and an alloy pellet, and R_3 correlates with the resistance between the particles in the pellet. In Fig. 7 and Table 5, R_1 generally increases with the increasing cycling because of the changing electrolyte content. R_2 varies within a small range with the progression of cycling, indicating that the doping of carbonyl Ni powders into the electrodes effectively improves the electrical contact between the alloy's particles and a current collector. R_3 and R_{ct} show similar variation trends during the cycling: they first decrease, then increase, and then decrease again.

As described above, the reaction resistance R_{ct} is changed, due to the variations in the reactivity at the surface of the alloy and changes in the reacting area due to the particle disintegration of the alloy. With increasing cycling, R_{ct} may decrease as a result of the increasing reaction area but may also increase because of a small loss in the amount of the rechargeable alloy particles. The significant growth of R_{ct} as the cycle number is increased up to 350 results in a tremendous capacity loss. Furthermore, when the cycle number is enhanced to 500, a profound pulverization of the electrodes happens which results in a decrease of R_{ct}.

In summary, the deterioration mechanism of the Ti/Zr-based AB_2 alloys is related to the decreased reactivity at the alloy surface and a poor contact between the alloy particles originating from the pulverization of the alloy, as clearly demonstrated by the performed electrochemical experiments.

4. Conclusions

The La-doped Zr/Ti-based AB_2-type alloys with different Ti/Zr ratios were studied through XRD, SEM/EDX, NPD, and electrochemical measurements. The XRD data show that all the alloys contain a C15 Laves-type intermetallic as the major phase. Both the unit cell parameter *a* and the volume of the unit cell *V* follow the Vegard's law of proportionality vs content of Ti when a contraction of the structure is taking place. The metallurgical characterization results demonstrate that the La–Ni phase is present as the secondary phase in the annealed alloys. The LaNi phase, even in minor amounts, plays a vital role in facilitating the activation of the alloys.

The neutron diffraction study on the deuteride $(Ti,Zr,V)(Ni,Mn,Fe,V)_2D_{3.2}$, which also crystallized with a C15-type structure, shows the occupation by D atoms of one type of the tetrahedral interstitial sites, namely, 96*g* sites with A_2B_2 surrounding, whereas the V atoms are located at the 8*a* and 16*d* sites.

As inferred from the electrochemical characterization data, the Ti12/Zr88 alloy presents the maximum discharge capacity (466 mAh/g), whereas the Ti22/Zr78 alloy displays a superior cycling stability and the best HRD performance. The good cycling stability of the Ti22/Zr78 alloy can be ascribed to the excellent corrosion resistance of the Ti having the highest contents in this alloy among all studied materials. Excellent HRD performance of the Ti22/Zr78 alloy is mainly due to the high hydrogen bulk diffusion coefficient in its hydride and low impedance of the anode electrode.

The deterioration of the cycling stability of the studied alloy is ascribed to the lowered reactivity at the alloy's surface and a poor contact between the alloy's particles due to the pulverization.

The findings of this work would be useful to optimize and to improve the electrochemical performance of the C15-based Laves type AB_2 alloys. The results of the present study show that an AB_2 anode alloy with advanced electrochemical performance can be obtained by optimizing the ratio between Ti and Zr.

CRediT authorship contribution statement

ChuBin Wan: Investigation, Formal analysis, Visualization, Writing – original draft, Writing – review & editing, Funding acquisition. **R.V. Denys:** Investigation, Formal analysis. **V.A. Yartys:** Conceptualization, Supervision, Writing – review & editing, Project administration, Funding acquisition.

Declaration of Competing Interest

The authors declare that they have no known competing financial interests or personal relationships that could have appeared to influence the work reported in this paper.

Acknowledgements

This study was funded by the Norwegian Research Council (project "High Power Batteries Probed by Neutron Scattering", program SYNKNØYT).

This work was also funded by the National Natural Science Foundation of China (Grant No. 11975043). C.B. Wan thanks the funding from the China Scholarship Council (CSC) (project No. 201506465019). We sincerely thank Dr. Denis Cheptiakov for his help during the NPD experiments performed at PSI.

Appendix A. Supporting information

Supplementary data associated with this article can be found in the online version at doi:10.1016/j.jallcom.2021.161655.

References

[1] L. Ouyang, J. Huang, H. Wang, J. Liu, M. Zhu, Progress of hydrogen storage alloys for Ni-MH rechargeable power batteries in electric vehicles: A review, Mater. Chem. Phys. 200 (2017) 164–178.
[2] Y. Liu, H. Pan, M. Gao, Q. Wang, Advanced hydrogen storage alloys for Ni/MH rechargeable batteries, J. Mater. Chem. 21 (2011) 4743–4755.
[3] S. Tan, Y. Shen, E. Onur Şahin, D. Noréus, T. Öztürk, Activation behavior of an AB_2 type metal hydride alloy for NiMH batteries, Int. J. Hydrog. Energy 41 (2016) 9948–9953.
[4] K.H. Young, J. Nei, C. Wan, R.V. Denys, V.A. Yartys, Comparison of C14- and C15-predomiated AB_2 metal hydride alloys for electrochemical applications, Batteries 3 (2017) 22.
[5] R. Li, J. Wan, F. Wang, C. Ding, R. Yu, Effect of non-stoichiometry on microstructure and electrochemical performance of $La_{0.8}Gd_xMg_{0.2}Ni_{3.15}Co_{0.25}Al_{0.1}$ (x = 0–0.4) hydrogen storage alloys, J. Power Sources 301 (2016) 229–236.
[6] T. Erika, F. Ricardo, R. Fabricio, Z. Fernando, D. Verónica, Electrochemical and metallurgical characterization of $ZrCr_{1-x}NiMo_x$ AB_2 metal hydride alloys, J. Alloy. Compd. 649 (2015) 267–274.
[7] J. Nei, K. Young, S.O. Salley, K.Y.S. Ng, Determination of C14/C15 phase abundance in Laves phase alloys, Mater. Chem. Phys. 136 (2012) 520–527.
[8] S.R. Ovshinsky, M.A. Fetcenko, J. Ross, A nickel metal hydride battery for electric vehicles, Science 260 (1993) 176–181.
[9] C. Wan, X. Jiang, Y. Qi, X. Ju, Effects of V substitution and annealing on Zr-based AB_2 alloys as anode material of metal hydride batteries, Intermetallics 127 (2020) 106979.
[10] A.A. Volodin, R.V. Denys, C. Wan, I.D. Wijayanti, Suwarno, B.P. Tarasov, V.E. Antonov, V.A. Yartys, Study of hydrogen storage and electrochemical properties of AB2-type $Ti_{0.15}Zr_{0.85}La_{0.03}Ni_{1.2}Mn_{0.7}V_{0.12}Fe_{0.12}$ alloy, J. Alloy. Compd. 793 (2019) 564–575.
[11] Y.Z. Chen, H.L. Pang, H. Wang, J.W. Liu, L.Z. Ouyang, M. Zhu, Exploration of Ti substitution in AB_2-type YZrFe based hydrogen storage alloys, Int. J. Hydrog. Energy 44 (2019) 29116–29122.
[12] Y.L. Du, X.G. Yang, Q.A. Zhang, Y.Q. Lei, M.S. Zhang, Phase structures and electrochemical properties of the Laves phase hydrogen storage alloys $Zr_{1-x}Ti_x(Ni_{0.6}Mn_{0.3}V_{0.1}Cr_{0.05})_2$, Int. J. Hydrog. Energy 26 (2001) 333–337.
[13] J. Huot, E. Akiba, T. Ogura, Y. Ishido, Crystal structure, phase abundance and electrode performance of Laves phase compounds (Zr, A)$V_{0.5}Ni_{1.1}Mn_{0.2}Fe_{0.2}$ (A = Ti, Nb or Hf), J. Alloy. Compd. 218 (1995) 101–109.
[14] K. Shu, S. Zhang, Y. Lei, G. Lü, Q. Wang, Effect of Ti on the structure and electrochemical performance of Zr-based AB_2 alloys for nickel–metal rechargeable batteries, J. Alloy. Compd. 349 (2003) 237–241.
[15] J.C. Sun, S. Li, S.J. Ji, Phase composition and electrochemical performances of the $Zr_{1-x}Ti_xCr_{0.4}Mn_{0.2}V_{0.1}Ni_{1.3}$ alloys with 0.1 < x < 0.3, J. Alloy. Compd. 404–406 (2005) 687–690.
[16] J.C. Sun, S. Li, S.J. Ji, The effects of the substitution of Ti and La for Zr in $ZrMn_{0.7}V_{0.2}Co_{0.1}Ni_{1.2}$ hydrogen storage alloys on the phase structure and electrochemical properties, J. Alloy. Compd. 446–447 (2007) 630–634.
[17] F.C. Ruiz, E.B. Castro, H.A. Peretti, A. Visintin, Study of the different ZrxNiy phases of Zr-based AB_2 materials, Int. J. Hydrog. Energy 35 (2010) 9879–9887.

[18] K. Young, T. Ouchi, B. Huang, B. Chao, M.A. Fetcenko, L.A. Bendersky, K. Wang, C. Chiu, The correlation of C14/C15 phase abundance and electrochemical properties in the AB_2 alloys, J. Alloy. Compd. 506 (2010) 841–848.
[19] J.M. Joubert, M. Latroche, A. Percheron-Guégan, J. Bouet, Improvement of the electrochemical activity of Zr-Ni-Cr Laves phase hydride electrodes by secondary phase precipitation, J. Alloy. Compd. 240 (1996) 219–228.
[20] K. Young, T. Ouchi, X. Lin, B. Reichman, Effects of Zn-addition to C14 metal hydride alloys and comparisons to Si, Fe, Cu, Y, and Mo-additives, J. Alloy. Compd. 655 (2016) 50–59.
[21] K. Young, T. Ouchi, B. Huang, B. Reichman, M.A. Fetcenko, The structure, hydrogen storage, and electrochemical properties of Fe-doped C14-predominating AB_2 metal hydride alloys, Int. J. Hydrog. Energy 36 (2011) 12296–12304.
[22] Y. Zhu, H. Pan, M. Gao, Y. Liu, Q. Wang, A study on improving the cycling stability of $(Ti_{0.8}Zr_{0.2})(V_{0.533}Mn_{0.107}Cr_{0.16}Ni_{0.2})_4$ hydrogen storage electrode alloy by means of annealing treatment:: I. Effects on the structures, J. Alloy. Compd. 347 (2002) 279–284.
[23] M. Bououdina, C. Lenain, L. Aymard, J.L. Soubeyroux, D. Fruchart, The effects of heat treatments on the microstructure and electrochemical properties of the $ZrCr_{0.7}Ni_{1.3}$ multiphase alloy, J. Alloy. Compd. 327 (2001) 178–184.
[24] W.K. Zhang, C.A. Ma, X.G. Yang, Y.Q. Lei, Q.D. Wang, G.L. Lu, Influences of annealing heat treatment on phase structure and electrochemical properties of $Zr(MnVNi)_2$ hydrogen storage alloys, J. Alloy. Compd. 293–295 (1999) 691–697.
[25] H. Kim, M. Faisal, S.I. Lee, J.Y. Jung, H.J. Kim, J. Hong, Y.S. Lee, J.H. Shim, Y.W. Cho, D.H. Kim, J.Y. Suh, Activation of Ti–Fe–Cr alloys containing identical AB_2 fractions, J. Alloy. Compd. 864 (2021) 158876.
[26] C. Wan, X. Jiang, X. Yin, X. Ju, High-capacity Zr-based AB_2-type alloys as metal hydride battery anodes, J. Alloy. Compd. 828 (2020) 154402.
[27] S. Chang, K. Young, J. Nei, T. Ouchi, X. Wu, Effects of lithium addition in AB_2 metal hydride alloy by solid-state diffusion, Int. J. Hydrog. Energy 44 (2019) 29319–29328.
[28] M.W. Davids, T. Martin, M. Lototskyy, R. Denys, V. Yartys, Study of hydrogen storage properties of oxygen modified Ti- based AB_2 type metal hydride alloy, Int. J. Hydrog. Energy 46 (2021) 13658–13663.
[29] A.C. Larson, R.B.V. Dreele, General structure analysis system (GSAS), Los Alamos Natl. Lab. Rep. LAUR (1994) 86–748.
[30] P. Fischer, G. Frey, M. Koch, M. Könnecke, V. Pomjakushin, J. Schefer, R. Thut, N. Schlumpf, R. Bürge, U. Greuter, S. Bondt, E. Berruyer, High-resolution powder diffractometer HRPT for thermal neutrons at SINQ, Phys. B 276–278 (2000) 146–147.
[31] W.K. Hu, R.V. Denys, C.C. Nwakwuo, T. Holm, J.P. Maehlen, J.K. Solberg, V.A. Yartys, Annealing effect on phase composition and electrochemical properties of the Co-free La_2MgNi_9 anode for Ni-metal hydride batteries, Electrochim. Acta 96 (2013) 27–33.
[32] C. Wan, R.V. Denys, M. Lelis, D. Milčius, V.A. Yartys, Electrochemical studies and phase-structural characterization of a high-capacity La-doped AB_2 Laves type alloy and its hydride, J. Power Sources 418 (2019) 193–201.
[33] A.V. Irodova, G. Andre, F. Bouree, Hydrogen redistribution in the solid solutions ZrV_2D_x, $2.2 \le x \le 2.7$.: II. Structure of the intermediate phase: 'Lattice liquid crystal'. A neutron-diffraction study, J. Alloy. Compd. 350 (2003) 196–204.
[34] A.V. Skripov, J.C. Cook, D.S. Sibirtsev, C. Karmonik, R. Hempelmann, Quasielastic neutron scattering study of hydrogen motion in C15-type TaV_2H_x, J. Phys. Condens. Matter 10 (1998) 1787–1801.
[35] L.Z. Ouyang, Z.J. Cao, L.L. Li, H. Wang, J.W. Liu, D. Min, Y.W. Chen, F.M. Xiao, R.H. Tang, M. Zhu, Enhanced high-rate discharge properties of $La_{11.3}Mg_{6.0}Sm_{7.4}Ni_{61.0}Co_{7.2}Al_{7.1}$ with added graphene synthesized by plasma milling, Int. J. Hydrog. Energy 39 (2014) 12765–12772.
[36] X. Zhao, Y. Ding, L. Ma, L. Wang, M. Yang, X. Shen, Electrochemical properties of $MmNi_{3.8}Co_{0.75}Mn_{0.4}Al_{0.2}$ hydrogen storage alloy modified with nanocrystalline nickel, Int. J. Hydrog. Energy 33 (2008) 6727–6733.
[37] N. Kuriyama, T. Sakai, H. Miyamura, I. Uehara, H. Ishikawa, T. Iwasaki, Electrochemical impedance and deterioration behavior of metal hydride electrodes, J. Alloy. Compd. 202 (1993) 183–197.